Journal of Rock Mechanics and Geotechnical Engineering 15 (2023) 1476–1490

Contents lists available at ScienceDirect

Journal of Rock Mechanics and Geotechnical Engineering

journal homepage: www.jrmge.cn

Full Length Article

Dynamic behaviors of water-saturated and frozen sandstone subjected to freeze-thaw cycles

Feng Gao [a,b], Cong Li [a,b], Xin Xiong [a,b,*], Yanan Zhang [c], Keping Zhou [a,b]

[a] School of Resources and Safety Engineering, Central South University, Changsha, 410083, China
[b] Research Center for Mining Engineering and Technology in Cold Regions, Central South University, Changsha, 410083, China
[c] Department of Aerospace and Mechanical Engineering, The University of Arizona, Tucson, AZ, 85721, USA

ARTICLE INFO

Article history:
Received 15 June 2022
Received in revised form
6 October 2022
Accepted 14 November 2022
Available online 10 December 2022

Keywords:
Freeze-thaw (F-T) cycle damage
Dynamic properties
Split Hopkinson pressure bar (SHPB)
Increasing rate of porosity

ABSTRACT

In high-altitude cold areas, freeze-thaw (F-T) cycles induced by day-night and seasonal temperature changes cause numerous rock mass slope engineering disasters. To investigate the dynamic properties of rock in the natural environment of a high-altitude cold area, standard specimens were drilled from the slope of the Jiama copper mine in Tibet, and dynamic compression tests were performed on water-saturated and frozen sandstone with different numbers of F-T cycles (0, 10, 20, 30, and 40) by the split Hopkinson pressure bar (SHPB) system with a cryogenic control system. The influence of water-saturated and frozen conditions on the dynamic performance of sandstone was investigated. The following conclusions are drawn: (1) With increasing strain rate, the attenuation factor (λ_a) of water-saturated sandstone and the intensifying factor (λ_i) of frozen sandstone linearly increase. As the number of F-T cycles increases, the dependence factor (λ_d) of water-saturated sandstone linearly decreases, whereas the λ_d of frozen sandstone linearly increases. (2) The prediction equation of the dynamic compressive strength of water-saturated and frozen sandstone is obtained, which can be used to predict the dynamic compressive strength of sandstone after various F-T cycles based on the strain rate. (3) The mesoscopic mechanism of water-saturated and frozen sandstone's dynamic compressive strength evolution is investigated. The water softening effect causes the dynamic compressive strength of water-saturated sandstone to decrease, whereas the strengthening effect of pore ice causes it to increase. (4) The decrease in the relative dynamic compressive strength of water-saturated sandstone and the increase in the relative dynamic compressive strength of frozen sandstone can be attributed to the increased porosity.

1. Introduction

In high-altitude cold areas, freeze-thaw (F-T) cycles induced by day-night and seasonal temperature changes cause numerous rock mass engineering disasters, such as frost heave instability and cracking of tunnel surrounding rock (Lai et al., 2000), F-T denudation and collapse of rock slope (Matsuoka, 2008; Krautblatter et al., 2013), and F-T of material cultural heritage (Ruedrich et al., 2011; Al-Omari et al., 2015), which harms the design and construction of rock mass engineering. The strength and deformation properties of rock are the theoretical basis for evaluating the stability of rock mass engineering and optimizing the engineering design. Therefore, an investigation of the mechanical properties of rock after F-T cycle treatment is essential to ensure the safety of rock engineering and disaster prevention and mitigation in cold areas.

The law of rock strength deterioration under F-T cycles has been extensively analyzed. The results indicate that the uniaxial compressive strength (UCS) (Yavuz, 2011; Fener and İnce, 2015; Khanlari et al., 2015; Ince and Fener, 2016; Momeni et al., 2016; Wang et al., 2016a, b; Cui et al., 2017; Fang et al., 2018; Gao et al., 2021), Brazilian tensile strength (BTS) (Altindag et al., 2004; Jamshidi et al., 2013; Fener and İnce, 2015; Momeni et al., 2016; Zhang et al., 2019a), point load strength (PLS) (Altindag et al., 2004; Jamshidi et al., 2013; Fener and İnce, 2015; Ince and Fener, 2016), and elastic modulus (E) (Liu et al., 2011; Tan et al., 2011; Wang et al., 2016a, b; Fang et al., 2018; Gao et al., 2021) of rock after F-T cycles

* Corresponding author. School of Resources and Safety Engineering, Central South University, Changsha, 410083, China.
E-mail address: xiongxin@csu.edu.cn (X. Xiong).
Peer review under responsibility of Institute of Rock and Soil Mechanics, Chinese Academy of Sciences.

https://doi.org/10.1016/j.jrmge.2022.11.007

show an exponential decline trend with an increase in the number of F-T cycles but to different degrees. With an increase in the number of F-T cycles, the porosity of rock (Fener and İnce, 2015; Momeni et al., 2016; Gao et al., 2019) increases, but the P-wave velocity decreases (Luo et al., 2014; Fener and İnce, 2015; Momeni et al., 2016). The triaxial compression test of Wang et al. (2019) showed that under the same confining pressure condition, the triaxial compressive strength of the two sandstones decreases with an increase in F-T cycles, and an exponential decay relation is expressed. The friction angle (φ) is kept constant, and there is an excellent exponential decay relationship between the cohesion (C) and the F-T cycles. Liu et al. (2011) confirmed that the Poisson's ratio of rock presents a downward trend as the number of F-T cycles increases. The Poisson's ratio becomes negative when the number of F-T cycles reaches a certain degree. Niu et al. (2021) carried out a crack propagation gauge test. The results showed that as the number of F-T cycles increases, the crack initiation time nonlinearly decreases, and the increased amplitude gradually decreases. The crack propagation speed increases with an increase in the number of F-T cycles, causing a decrease in rock strength. Based on the elastic-plastic theory and fatigue damage mechanics, combined with rock's actual stress distribution under F-T cycles, Liu et al. (2015) proposed a prediction model for UCS that integrated the F-T cycle treatment. Based on the stress-strain curve characteristics of rock after F-T treatment and the viewpoint of statistical damage mechanics, Gao et al. (2021) proposed a piecewise constitutive model of rock after F-T treatment under uniaxial compression. However, the above research results mainly focused on the static characteristics of rock after F-T cycles. There is no doubt that actual rock mass engineering in cold areas is always in a complex engineering environment of excavation and blasting disturbance. To approach actual rock mass engineering, it is necessary to examine the dynamic properties of rocks before and after F-T cycles.

Recently, the dynamic properties of rocks after F-T cycles have been increasingly analyzed. The results indicate that both the dynamic UCS (UCS_d) (Wang et al., 2016a, b; Ke et al., 2018; Li et al., 2018; Liu et al., 2018; Ma et al., 2018; Zhang et al., 2019b; Weng et al., 2020) and dynamic Brazilian splitting strength (BTS_d) (Liu et al., 2018; Weng et al., 2020) decrease with increasing F-T cycles but to different degrees. Liu et al. (2021) discovered that as the number of F-T cycles increases, the dynamic elastic modulus (E_d) linearly decreases, while the peak strain nonlinearly increases. The deformation resistance of rock specimens decreases after F-T cycle treatment, and the deformation easily occurs under dynamic loading. Zhou et al. (2015) divided the dynamic compressive stress-strain curve of sandstone into four stages after the F-T cycles, and found that the compressive stress-strain curve at the compaction stage is less evident than that at the static stage. Weng et al. (2020) investigated the effect of moisture on the dynamic properties of granite during F-T cycles and discovered that the dynamic tensile strength and compressive strength of sealed-dried specimens are higher than those of semi-immersed or completely immersed specimens during F-T cycles. The dynamic F-T damage coefficient (K_{df}) and F-T damage variable (D) were defined by Ma et al. (2018). With the same F-T cycles, the K_{df} of mudstone is greater than that of sandy mudstone. D is negatively correlated with the dynamic UCS of mudstone and sandy mudstone. Liu et al. (2018) performed a dynamic Brazilian splitting test on granite after F-T cycles, and the results revealed that the frost heave force caused by the F-T cycles promotes the expansion of microdefects in granite. These microdefects were easier to expand under dynamic loading, which was the primary cause of the decline in dynamic tensile strength. To describe the increase in dynamic strength caused by the strain rate increase, Ke et al. (2018) developed a dynamic increase factor (DIF) model by the attenuation model and proposed dynamic strength deterioration equations for various types of rocks with different numbers of F-T cycles. The above research results primarily focused on the dynamic properties of rock subjected to the F-T cycles in a water-saturated state.

However, in addition to repeated F-T cycles, the actual engineering rock mass in cold regions may be subject to short-term freezing (winter) or short-term saturation (summer) due to the effect of seasons. Selecting the Jiama copper mine in Tibet as an example, Fig. 1a shows the daily maximum and minimum temperature change curves of the mine in Mozhugongka within five years. The maximum and minimum temperatures periodically change, which will induce the rock mass of the mine to undergo repeated F-T cycles. Fig. 1b shows the change characteristics of the position of the seasonally frozen layer of the open pit slope with slope excavation. With increasing excavation depth, the original permanent frozen layer and unfrozen layer transform into the seasonally frozen layer, i.e. the slope rock mass undergoes different F-T cycles under periodic temperature changes. However, Fig. 1a shows that one year can also be divided into a freezing period, transition period, and thawing period, according to the characteristics of temperature change. Therefore, the seasonally frozen layer of the slope in Fig. 1b will be in the period of freezing or thawing saturation. As shown in Fig. 1c, during the thawing period, the seasonally frozen layer of the slope is in a water-saturated state; during the freezing period, the seasonally frozen layer of the slope is completely frozen. Török et al. (2019) discovered that frozen rock filled with pore ice improves the UCS of porous rock and has completely different mechanical properties than water-saturated rock. In practice, using these mechanical models may cause inaccurate or even large deviations in the characterization of the mechanical behavior of rock excavation in cold regions. As a result, in-depth research on the dynamic properties of water-saturated and frozen rock after F-T cycle treatment is needed.

In this study, water-saturated sandstone specimens, which were obtained from the slope of the Jiama copper mine, were subjected to different quantities of F-T cycles, and the change laws in the T_2 spectrum distribution curves of sandstone specimens before and after F-T cycles were investigated. The dynamic compression tests of sandstone treated by F-T cycles in different states (i.e. water-saturated and frozen) were carried out to simulate the rock engineering and blasting vibration of the seasonally frozen layer of the slope in the cold region. The stress-strain curve characteristics and strength evolution law of water-saturated and frozen sandstone were investigated for various F-T cycles and strain rates. A dynamic compressive strength evolution model of coupling F-T cycles and strain rates was developed. The mesoscopic mechanism of the dynamic compressive strength evolution of water-saturated and frozen sandstone was investigated.

2. Experimental materials and methods

2.1. Rock specimen preparation

There were no visible cracks or developed joints on the surface of the sandstone specimens obtained from the open pit slope of the Jiama copper mine in Tibet. According to the rock mechanics test requirements proposed in Ulusay (2015), a sandstone specimen was processed in a cylinder with a diameter of 50 mm and a height of 50 mm. The prepared sandstone specimens were dried in an air-blast drying chamber until their mass reached a constant value, at which point the rock specimens were considered "completely dry". The basic physical parameters and population standard deviation of the specimens are listed in Table 1. The nuclear magnetic resonance (NMR) porosity test refers to the standard SY/T 6490-2007 (2007), and the P-wave test refers to the standards SY/T 6351-1998 (1998)

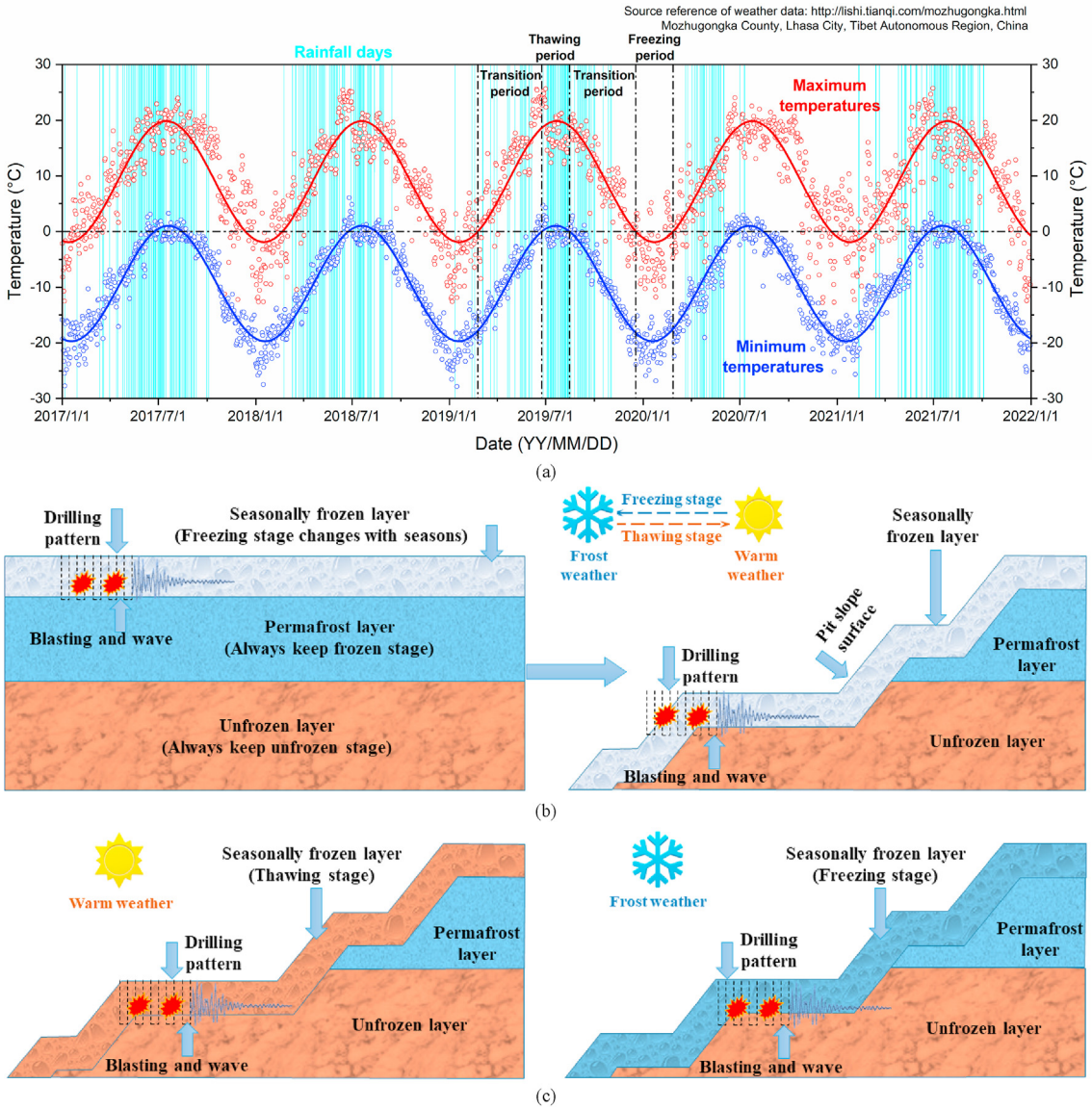

Fig. 1. Open pit slope engineering in cold regions: (a) Maximum and minimum temperature changes in Mozhugongka County, Lhasa, Tibet Autonomous Region, China; (b) Before and after open pit slope excavation; and (c) Changes in the seasonally frozen layer in warm and frost weather.

and SL/T 264-2020 (2020). The mineral composition of sandstone is shown in Fig. 2.

2.2. Experimental apparatus

The main experimental apparatus utilized in the test is described as follows:

(1) Vacuum pressurization saturation device (type ZYB-II): The vacuum pressurization saturation device mainly uses a vacuum device to vacuum the core and then adds a certain specification of liquid (e.g. water) in the vacuum state for soaking so that the core can be fully absorbed. The vacuum pumping rate is 2 L/min, and the pumping time can be determined according to the compactness of the rock specimens.

(2) F-T cycle tester (type TDS-300): The F-T cycle tester adopts the method of freezing in air and thawing in water to conduct periodic freezing and thawing tests. With a high degree of automation, one set can automatically complete multiple F-T cycle tests. During the F-T test, the temperature difference at each point inside the testing machine was less than 2 °C, with a 0.5 °C measurement accuracy.

(3) Rock NMR analysis system (type AniMR-150): NMR testing technology is a non-destructive testing method based on the condition that water enters the rock pores. ^{1}H protons change from a high-energy state to a low-energy state in a non-radiative way, referred to as relaxation. Spin-lattice relaxation, i.e. longitudinal relaxation, reduces the overall energy of magnetic nuclei, while spin-spin relaxation, i.e. transverse relaxation, does not reduce the overall energy of magnetic nuclei. In this study, the Carr-Purcell-Meiboom-Gill (CPMG) spin-echo sequence in the MacroME12-150H-I-60 mm was employed to test the transverse relaxation time of the specimens. By measuring the transverse relaxation time of water-saturated rock specimens, the porosity and T_2 spectrum distribution curves of the specimens can be

Table 1
Basic physical parameters of 40 sandstone specimens.

Physical parameter	Value	Population standard deviation, σ
Average drying mass (g)	222.91	2.72
Average height (mm)	50.08	0.17
Average diameter (mm)	49.88	0.301
Average initial porosity (%)	8.36	0.058
Average P-wave velocity (m/s)	2731	238.8

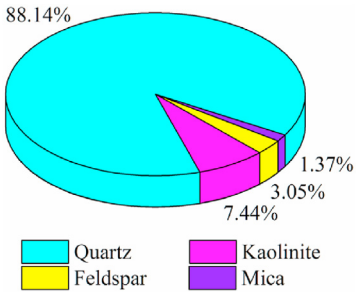

Fig. 2. Mineral composition of sandstone specimens.

obtained. The main parameters of the CPMG spin-echo sequence set in this study are listed in Table 2.

(4) Cryogenic test chamber (type DW-25): The temperature control accuracy of the cryogenic test chamber is ±2 °C, which was utilized for the temporary storage of saturated frozen sandstone specimens. There are wheels at the bottom of the test chamber, which can easily transport frozen rock specimens to prevent the specimens from melting before the tests.

(5) Split Hopkinson pressure bar (SHPB): Considering the effect of ambient temperature on the experimental results, the dynamic experimental device has been modified to better complete this test.

2.3. Test procedures

2.3.1. F-T cycle test

Based on the local climate of the mine site (Gao et al., 2021), one F-T cycle in all tests is designed as 10 h, including 4 h for freezing water-saturated sandstone specimens at −20 °C, 4 h for thawing in water at 20 °C, and 2 h for cooling and warming.

The specific test steps are described as follows:

(1) All sandstone specimens were dried and marked, as shown in Table 3.

(2) The sandstone specimens were vacuum water-saturated at 0.1 MPa with 2 h of dry pumping and 1 h of wet pumping. The sandstone specimens were removed after vacuum saturation and soaked in water for 48 h to saturate the specimen thoroughly.

Table 2
Main parameters of the CPMG spin-echo sequence.

Main magnetic field (T)	Frequency of radio pulse (MHz)	Waiting time (s)	Echo time (ms)	Echo number	Cumulative sampling number
0.5 ± 0.03	12	3.5	0.15	8192	32

Table 3
Specimen IDs for water-saturated and frozen sandstone specimens.

Number of F-T cycles	Specimen ID			
	0.4 MPa	0.5 MPa	0.6 MPa	0.7 MPa
0	CA1, CA3	CA5, CA7	CA9, CA11	CA13, CA15
10	CB1, CB3	CB5, CB7	CB9, CB11	CB13, CB15
20	CC1, CC3	CC5, CC7	CC9, CC11	CC13, CC15
30	CD1, CD3	CD5, CD7	CD9, CD11	CD13, CD15
40	CE1, CE3	CE5, CE7	CE9, CE11	CE13, CE15

Note: Impact gas pressures are 0.4 MPa, 0.5 MPa, 0.6 MPa and 0.7 MPa.

(3) Before F-T treatment, the porosity of the water-saturated sandstone specimens was measured using an Ani-MR150 rock nuclear magnetic resonance imaging analysis system.

(4) As a control group, Group CA specimens were prepared directly. In addition, specimens from Groups CB, CC, CD, and CE were freeze-thawed for 10, 20, 30 and 40 F-T cycles, respectively, before dynamic tests.

(5) The corresponding sandstone specimens were removed after the specified number of F-T cycles had been completed, and Step (2) was repeated. The porosity of water-saturated sandstone specimens was then measured after F-T cycles.

(6) The water-saturated sandstone marked with 1, 5, 9 and 13 was subjected to a dynamic compression test. Water-saturated sandstones 3, 7, 11 and 15 were lightly wiped and wrapped in plastic film before being placed in a cryogenic test chamber and frozen at −20 °C for 48 h (the specimens were considered completely frozen), and then dynamic compression tests were performed.

The whole test procedure and experimental apparatus are illustrated in Fig. 3.

2.3.2. SHPB test

The SHPB at Central South University was used to test the rock dynamic properties. Considering the effect of ambient temperature on the experimental results, the SHPB experimental device was modified to achieve accurate maintenance of the frozen state and low temperature of sandstone during the experiment by adding a cryogenic test chamber, as shown in Fig. 4. The main body of the chamber was a custom-made plexiglass structure and can provide excellent airtightness after connecting to the SHPB device. Heat insulation material was applied to the outer wall to maintain the ambient temperature of the chamber effectively. To facilitate the movement of the incident bar and transmission bar, circular holes with a diameter slightly greater than 50 mm were opened on both sides of the box body. To prevent indoor air from influencing the temperature of the cryogenic test chamber, airtight material was wrapped around the circular hole. A loose-leaf door on the front side of the box makes it easy to place and remove specimens. A small hole was drilled on the top side of the box to allow access to the inside. Low-temperature nitrogen was transported from the liquid nitrogen container through the small hole to maintain a stable internal temperature in the box. The thermocouple was installed inside the box body to monitor temperature changes in real-time during the testing process with a 0.1 °C accuracy.

The SHPB compression tests on frozen sandstone specimens with different numbers of F-T cycles were carried out in a low-temperature environment test chamber under relatively stable temperature conditions, and the test data were recorded. An improved fusiform striker with a length of 360 mm was used in the SHPB to maintain the dynamic load with a constant strain rate. The incident bar, transmission bar and absorbing bar have a diameter of 50 mm and are composed of the same 40 Cr alloy steel as the punch.

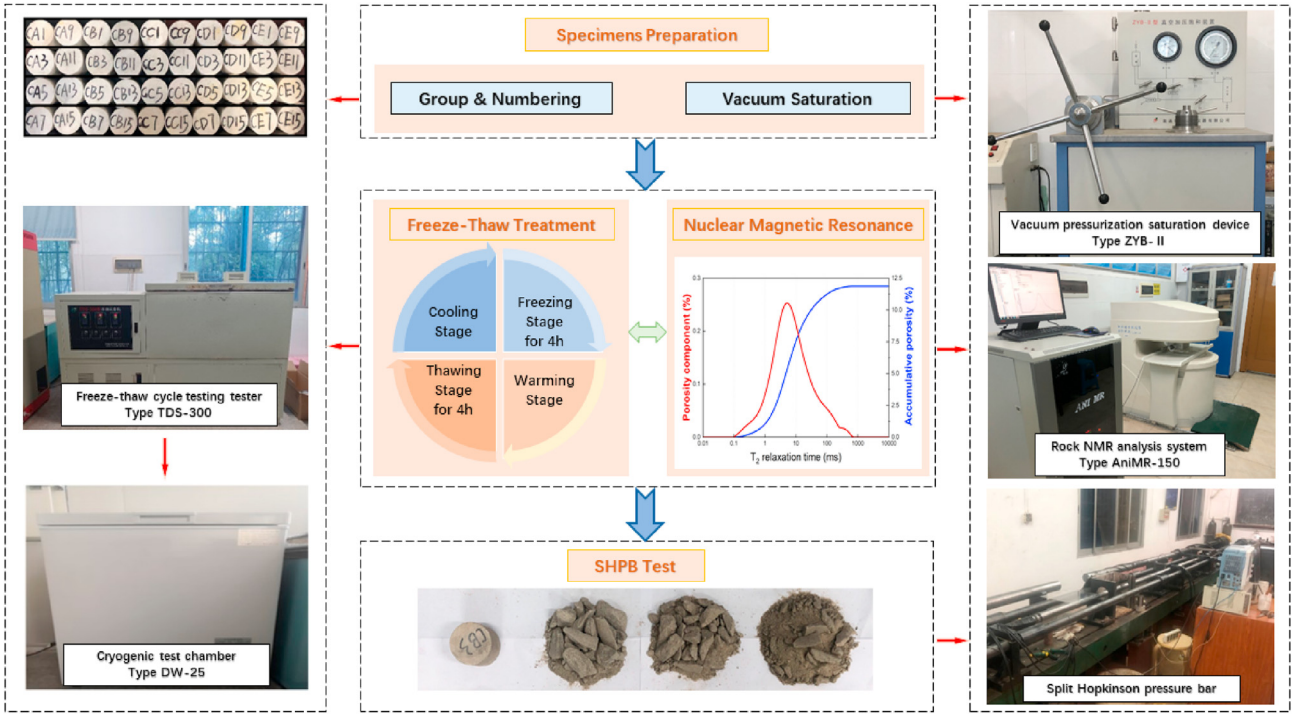

Fig. 3. Test procedures and experimental apparatus.

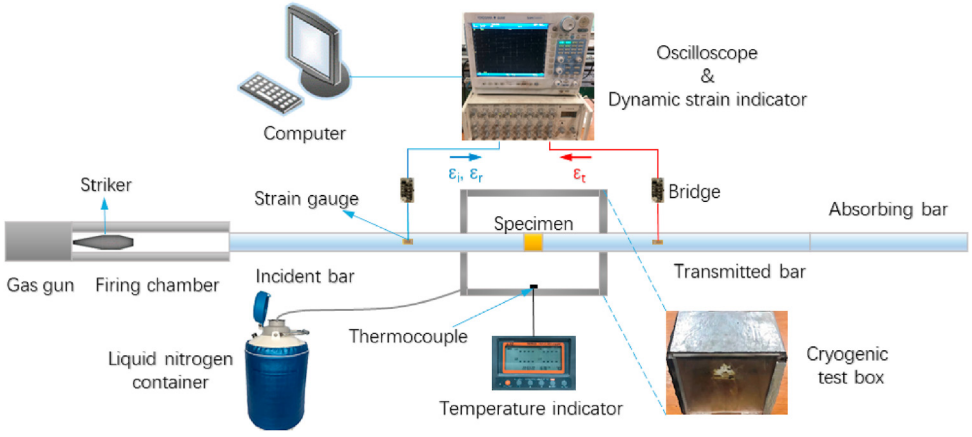

Fig. 4. Schematic diagram of the SHPB test system with cryogenic control. ε_i, ε_r and ε_t are the signal values of the incident, reflected and transmitted strains, respectively.

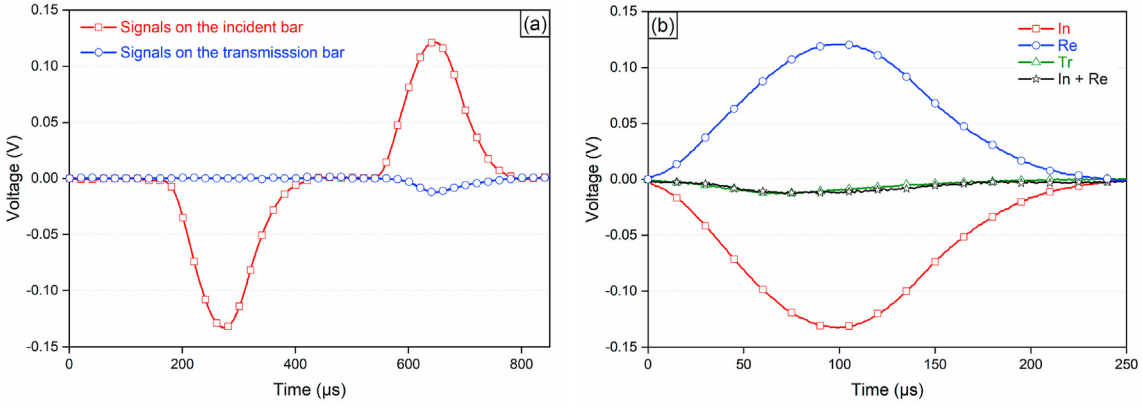

Fig. 5. (a) Signals on the bars, and (b) Signals reach stress equilibrium.

Petroleum jelly was smeared on the contact surface of the sandstone specimen with the incident and transmission bars before the test to ensure that incident and transmitted waves fully propagated at the interface.

2.3.3. Stress equilibrium

The essential requirement for effective reliable dynamic compression test is that the rock specimen reaches stress equilibrium before failure. Fig. 5a shows the strain gauge signals collected by the ultradynamic strain recorder on the incident and transmission bars, and Fig. 5b shows the electrical signals of the incident wave (In), reflected wave (Re) and transmitted wave (Tr) of sandstone specimens after data processing. The stress equilibrium of all specimens was rigorously evaluated.

During the SHPB test (Li et al., 2005, 2008), high-pressure gas drives the striker on the incident bar, generating an incident pulse rapidly transmitted to the sandstone specimen. A reverse reflected wave will be generated on the contact surface between the sandstone specimen and the incident bar due to different media, and a transmitted wave will be generated on the transmission bar during wave transmission from the incident bar to the specimen and transmission bar. The one-dimensional (1D) stress wave assumption must be satisfied during the SHPB test, which means that when the stress wave in the incident bar is transmitted forward, only the deformation generated along the stress wave transmission direction is considered, but the radial deformation is disregarded. According to the assumption of a 1D stress wave, the strain, strain rate and stress of the specimens can be obtained as follows:

$$\varepsilon = \frac{u_1 - u_2}{L_s} = \frac{C_e}{L_s}\int_0^t (\varepsilon_i - \varepsilon_r - \varepsilon_t)\mathrm{d}t \tag{1}$$

$$\dot{\varepsilon} = \frac{\mathrm{d}\varepsilon}{\mathrm{d}t} = \frac{C_e}{L_s}(\varepsilon_i - \varepsilon_r - \varepsilon_t) \tag{2}$$

$$\sigma = \frac{P_1 + P_2}{2A_s} = \frac{A_e E_e}{2A_s}(\varepsilon_i + \varepsilon_r + \varepsilon_t) \tag{3}$$

where ε, $\dot{\varepsilon}$ and σ are the strain, strain rate and stress of the specimen, respectively; u_1 and u_2 are the transverse displacements of the incident and transmission bars, respectively; A_e, C_e and E_e denote the cross-sectional area, P-wave velocity and elastic modulus of the SHPB, respectively; P_1 and P_2 are the forces acting on both ends of the sandstone specimen; and L_s and A_s denote the length and cross-sectional area of the specimen, respectively.

The strain rate ($\dot{\varepsilon}$) and dynamic compressive strength (σ_{cd}) are listed in Table 4. For different impact gas pressures, the strain rates of water-saturated sandstone are $86 \pm 5\ s^{-1}$, $104 \pm 5\ s^{-1}$, $125 \pm 5\ s^{-1}$ and $152 \pm 5\ s^{-1}$. The strain rates of the frozen sandstone are $94 \pm 5\ s^{-1}$, $111 \pm 5\ s^{-1}$, $134 \pm 5\ s^{-1}$ and $160 \pm 5\ s^{-1}$.

Table 4
SHPB test results.

State of specimens	Number of F-T cycles	Specimen ID	strain rate, $\dot{\varepsilon}$ (s^{-1})	Dynamic compressive strength, σ_{cd} (MPa)
Water-saturated	0	CA1	82.2	47.904
		CA5	101.1	51.371
		CA9	121.4	57.154
		CA13	147.6	62.175
	10	CB1	84	44.043
		CB5	103.9	47.826
		CB9	124.2	50.896
		CB13	149.5	55.661
	20	CC1	86.2	40.588
		CC5	105.1	43.742
		CC9	126	46.075
		CC13	151.5	49.311
	30	CD1	88.5	37.65
		CD5	107.6	39.733
		CD9	127.5	42.877
		CD13	152.6	45.909
	40	CE1	90.1	34.426
		CE5	108.2	36.267
		CE9	129.8	38.027
		CE13	154.9	40.976
Frozen	0	CA3	91.2	57.836
		CA7	108.7	62.204
		CA11	130.4	67.485
		CA15	156.5	72.885
	10	CB3	92.4	60.764
		CB7	110.7	65.349
		CB11	132.2	70.79
		CB15	157.6	76.782
	20	CC3	94.1	63.141
		CC7	111.8	68.595
		CC11	133.9	73.967
		CC15	159.2	81.638
	30	CD3	95.9	65.709
		CD7	113.1	71.14
		CD11	135.3	77.921
		CD15	160.8	86.069
	40	CE3	97.3	68.702
		CE7	114.5	74.379
		CE11	136.5	82.111
		CE15	162.2	90.339

3. Experimental results

3.1. Characteristics of stress-strain curves

Fig. 6 depicts the five stages of the typical stress-strain curve of rocks (Okubo and Fukui, 1996). The segment *OA* is the compaction stage, which means that the original rock cracks are gradually closing and the stress-strain curve is concave upwards. The segment *AB* is the elastic deformation stage, and the stress-strain curve is an approximately straight line. The segment *BC* begins to undergo plastic deformation, and the curve deviates from linearity. The segment *CD* is an unstable fracture development stage, in which the fracture continues to develop until the rock specimen is destroyed and the stress-strain curve becomes downward concave. The fracture continues to develop until the rock specimen is destroyed, and the stress-strain curve has a downward concave shape. The segment *DE* refers to the time after a fracture has formed and the rock has been broken.

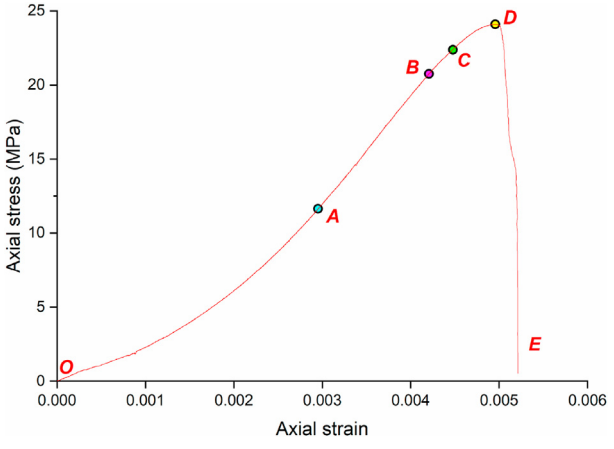

Fig. 6. Typical stress-strain curve of rocks.

In Fig. 6, stiffness refers to the ability of materials or structures to resist elastic deformation when subjected to force. The stiffness is usually measured by the elastic modulus, which represents the difficulty of the elastic deformation of rocks. The stiffness is related to the slope of the straight line at the initial part of the curve; the steeper the slope is, the greater the stiffness is. A parallel line is made with the straight line of the initial part of the curve at the point of crossing the curve. Comparing the intersection position of the parallel line and the *X*-axis, the greater the intersection value is, the better the plasticity is. Both the segments *BC* and *CD* represents the elastic-plastic stages. Compared with *AB*, the less steep the slope is, the more pronounced the plastic enhancement and the elastic attenuation are. Therefore, the performance of water-saturated and frozen sandstone can be roughly judged according to the trend of the dynamic stress-strain curve (Figs. 7 and 8).

The stress-strain curves for various impact gas pressures with the same number of F-T cycles are shown in Fig. 7. The dynamic compressive strength of water-saturated and frozen sandstone increases as the strain rate increases with the same number of F-T cycles. With an increase in the strain rate, the compaction stage of the dynamic compressive stress-strain curves for water-saturated sandstone becomes less visible, and the elastic modulus increases. Before reaching peak strength, the curves go through two stages: linear elasticity and elastoplasticity. The dynamic compressive stress-strain curves for frozen sandstone have no compaction stage, the elastic modulus increases as the strain rate increases, and the curves go through two stages of linear elasticity and elastoplasticity until the peak strength is reached. At the same number of F-T cycles, the stiffness of water-saturated and frozen sandstone increases with increasing strain rate. Next, the strength

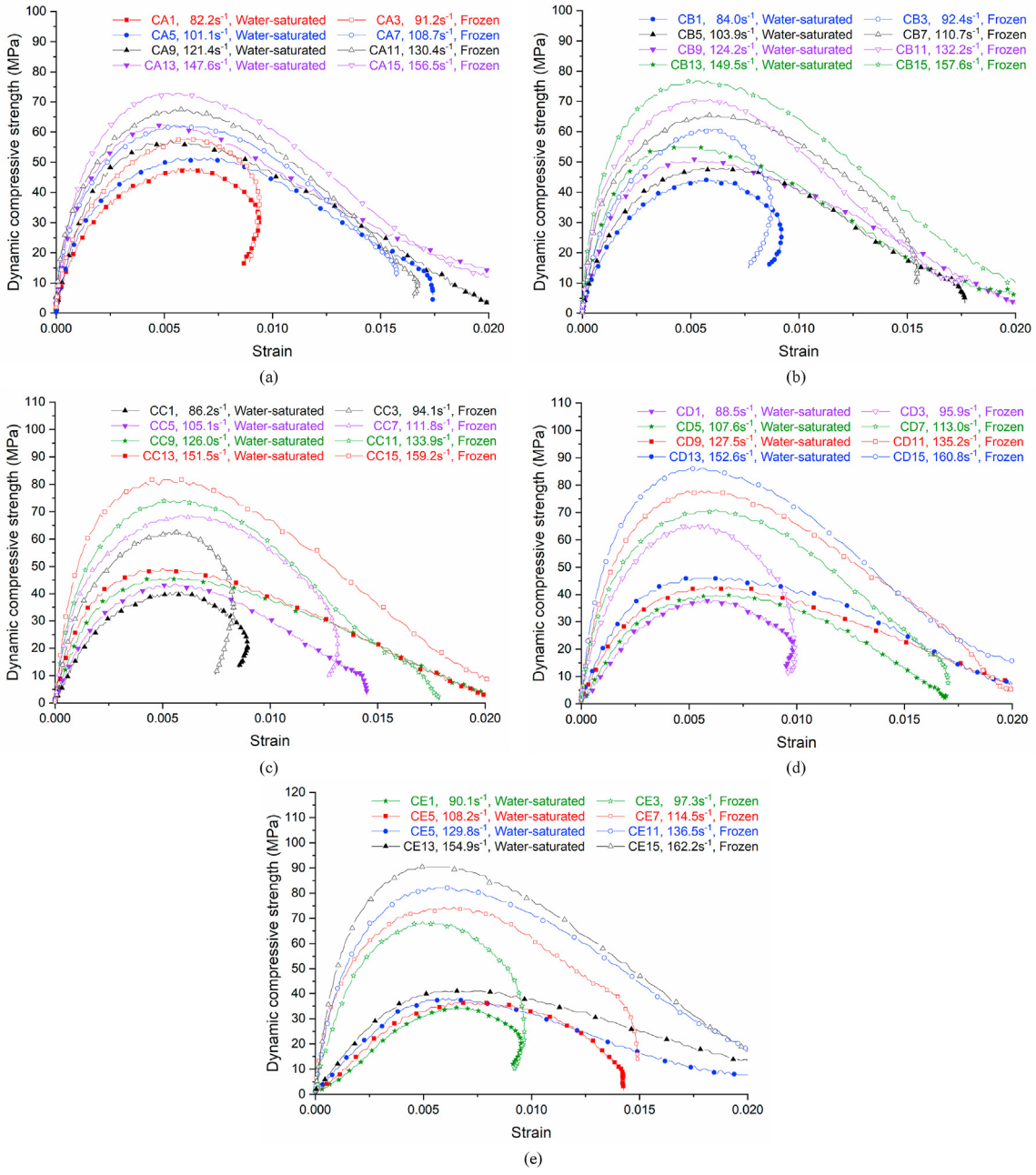

Fig. 7. Stress-strain curves of the specimens at the same F-T cycles and the different impact gas pressures: (a) 0 cycle, (b) 10 cycles, (c) 20 cycles, (d) 30 cycles, and (e) 40 cycles.

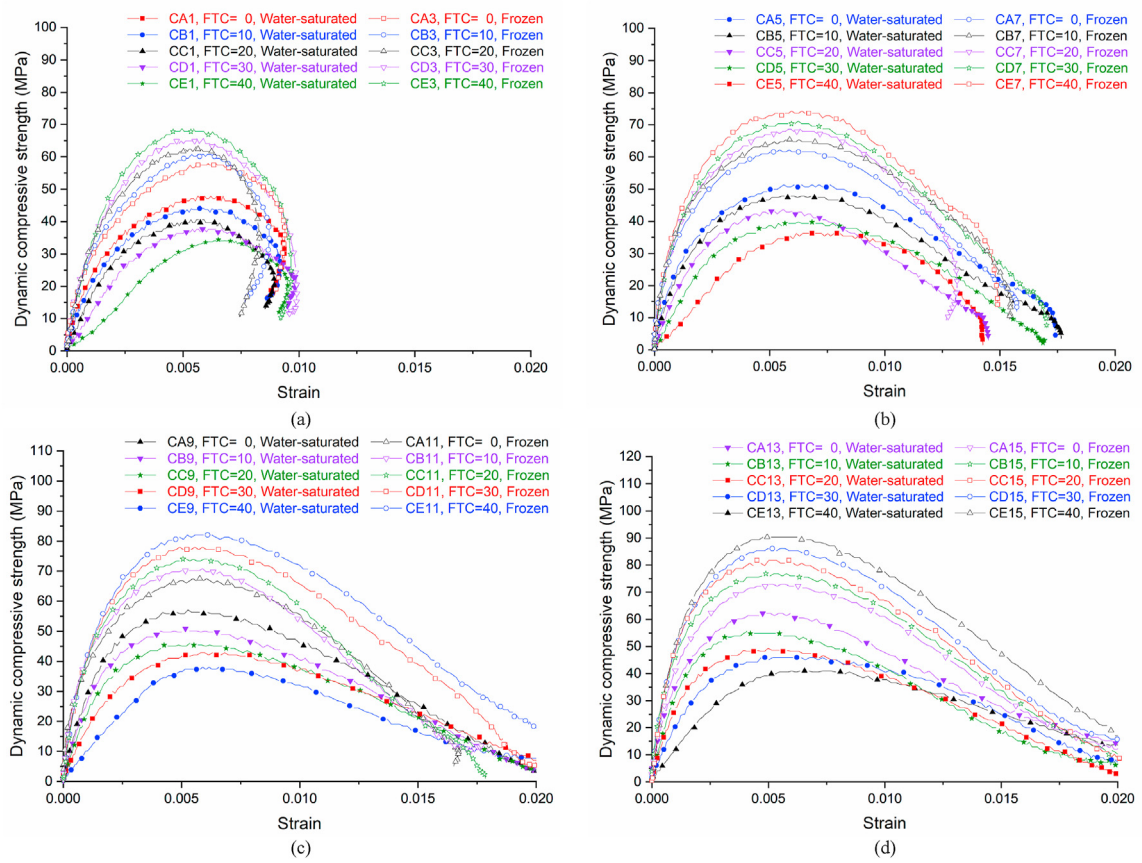

Fig. 8. Stress-strain curves of the specimens at different numbers of F-T cycles and the same impact gas pressures: (a) Strain rate of 86 ± 5 s^{-1} for water-saturated specimen and 94 ± 5 s^{-1} for frozen specimen, (b) Strain rate of 104 ± 5 s^{-1} for water-saturated specimen and 111 ± 5 s^{-1} for frozen specimen, (c) Strain rate of 125 ± 5 s^{-1} for water-saturated specimen and 134 ± 5 s^{-1} for frozen specimen, and (d) Strain rate of 152 ± 5 s^{-1} for water-saturated specimen and 160 ± 5 s^{-1} for frozen specimen.

drop rate of the sandstone with a low strain rate is faster than that of the sandstone with a high strain rate, regardless of water-saturated or frozen sandstone specimens. This finding indicates that the strength loss efficiency of sandstone with a low strain rate is also faster than that of sandstone with a high strain rate.

The dynamic stress-strain curves of sandstone with the same impact pressure are shown in Fig. 8. The dynamic compressive strength of water-saturated sandstone with the same strain rate decreases as the number of F-T cycles increases. The elastic modulus only slightly decreases from 0 to 10 cycles, and then the stress-strain curves gradually appear at the compaction stage as the number of F-T cycles increases, representing the gradual development of microcracks in the rock. The frozen sandstone similarly behaves, but there is no prominent compaction stage. At the same strain rates, the stiffness of water-saturated sandstone decreases with an increase in the number of F-T cycles, but the stiffness of frozen sandstone increases. Moreover, the decreasing rate of stiffness of water-saturated sandstone rapidly increases with an increase in the number of F-T cycles, but the increase in the stiffness of frozen sandstone is not apparent.

3.2. Variations of dynamic compressive strength

To analyze the influences of the number of F-T cycles and impact pressures on the properties of sandstone, the exponential decay model (Mutlutürk et al., 2004) can be used to perform the regression analysis of the evolution law, as written by

$$\frac{\sigma_{S,(n)}}{\sigma_{S,(0)}} = e^{-\lambda_a(\dot{\varepsilon})n} \tag{4}$$

$$\frac{\sigma_{F,(n)}}{\sigma_{F,(0)}} = e^{\lambda_i(\dot{\varepsilon})n} \tag{5}$$

where λ_a and λ_i denote the attenuation factor and the intensifying factor, respectively; n is the number of F-T cycles; $\sigma_{S,(n)}$ and $\sigma_{S,(0)}$ are the dynamic compressive strengths of water-saturated sandstone after n F-T cycles and before F-T cycles, respectively; and $\sigma_{F,(n)}$ and $\sigma_{F,(0)}$ are the dynamic compressive strengths of frozen sandstone after n F-T cycles and before F-T cycles, respectively.

Fig. 9a and b depicts the dynamic compressive strength of water-saturated and frozen sandstone specimens as a function of the number of F-T cycles under various impact pressures. As shown in Fig. 9a, the dynamic compressive strength of water-saturated sandstone gradually decreases as the number of F-T cycles increases under the same impact pressure. The attenuation factors (λ_a) are 0.00817, 0.00901, 0.00982 and 0.01053 for strain rates of 86 ± 5 s^{-1}, 104 ± 5 s^{-1}, 125 ± 5 s^{-1} and 152 ± 5 s^{-1}, respectively, i.e. the attenuation factor (λ_a) increases with increasing strain rate.

The dynamic compressive strength of frozen sandstone increases with an increase in the number of F-T cycles under the same impact pressure, as shown in Fig. 9b. The intensifying factors (λ_i) of the frozen sandstone specimens are 0.00421, 0.00439, 0.00488 and 0.00541, respectively, corresponding to the strain rates of 94 ± 5 s^{-1}, 111 ± 5 s^{-1}, 134 ± 5 s^{-1} and 160 ± 5 s^{-1}, i.e. the intensifying

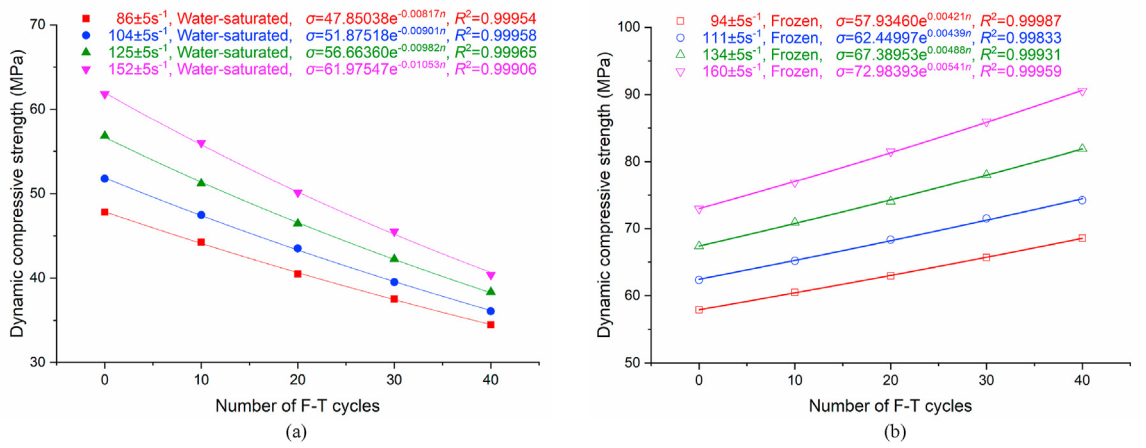

Fig. 9. Relationships between dynamic compressive stress and the number of F-T cycles: (a) Water-saturated specimens, and (b) Frozen specimens.

factor (λ_i) increases with increasing strain rate, and the increase rate gradually increases.

The attenuation factor (λ_a) is used to characterize the decreasing rate of the dynamic compressive strength of water-saturated sandstone under different strain rates. Fig. 10a shows that the attenuation factor (λ_a) linearly increases with increasing strain rate. By using regression analysis, the relationship between the attenuation factor (λ_a) and the strain rate can be obtained, as shown in Eq. (6). Under different strain rates, the intensifying factor (λ_i) is employed to characterize the decreasing rate of the dynamic compressive strength of frozen sandstone. As shown in Eq. (7), a regression analysis is performed to determine the intensifying factor (λ_i) of frozen sandstone from Fig. 10b. The intensifying factor (λ_i) linearly increases with increasing strain rate, similar to the attenuation factor (λ_a).

$$\lambda_a(\dot{\varepsilon}) = 3.55938\dot{\varepsilon} + 0.00523 \quad \left(R^2 = 0.97463\right) \tag{6}$$

$$\lambda_i(\dot{\varepsilon}) = 1.88123\dot{\varepsilon} + 0.00237 \quad \left(R^2 = 0.98395\right) \tag{7}$$

Fig. 11a and b shows the dynamic compressive strength evolution characteristics of water-saturated and frozen sandstone specimens, respectively, with the strain rate for the same number of F-T cycles. The dynamic compressive strengths of the water-saturated and frozen sandstone specimens linearly increase with increasing strain rate. The relationship between the dynamic compressive strength and the strain rate can be fitted by a linear model, as written by

$$\sigma = \lambda_d \dot{\varepsilon} + \sigma' \tag{8}$$

where λ_d denotes the dependence factor and σ' is the corresponding stress constant.

A linear regression analysis reveals the dependence factors of the evolution law of water-saturated sandstone specimens are 0.217662, 0.18031, 0.14679, 0.12595 and 0.09192 when the numbers of F-T cycles are 0, 10, 20, 30 and 40, respectively. Thus, the dependence of the compressive strength on the strain rate decreases as the strain rate increases. The dependence factors (λ_d) of frozen sandstone specimens are 0.22974, 0.2528, 0.28238, 0.30982 and 0.33937, when the numbers of F-T cycles are 0, 10, 20, 30 and 40, respectively, i.e. the dependence of compressive strength increases as the strain rate increases.

The dependence factor is used to characterize the effect of the strain rate on the dynamic compressive strength of sandstone for different F-T cycles. As shown in Fig. 12, with the increase in strain rate, the dependence factor of water-saturated sandstone linearly decreases, whereas the dependence factor of frozen sandstone linearly increases. Due to the change in the strain rate, the dynamic compressive strengths of water-saturated and frozen sandstone specimens exhibit opposite properties. After linear regression

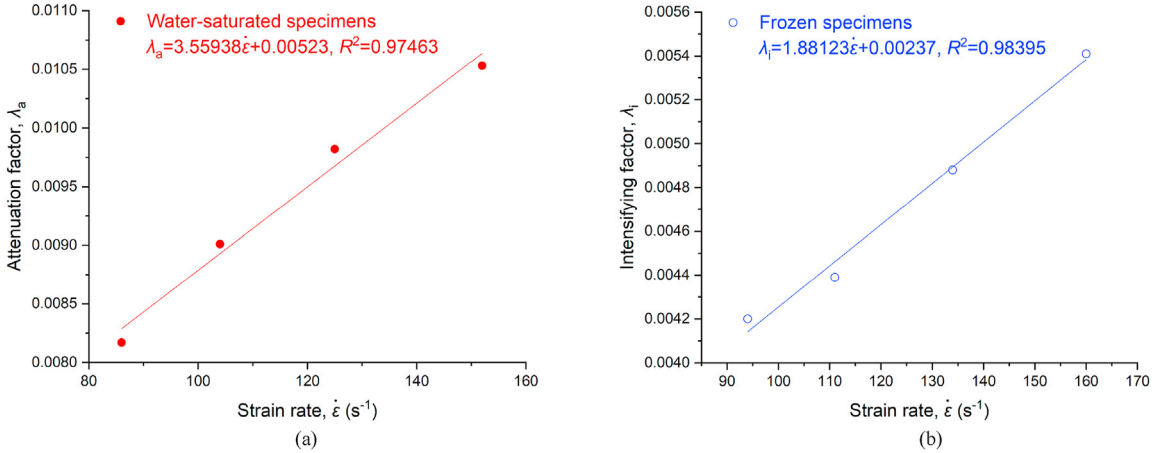

Fig. 10. Relationships among λ_a, λ_i and strain rate: (a) Water-saturated specimens, and (b) Frozen specimens.

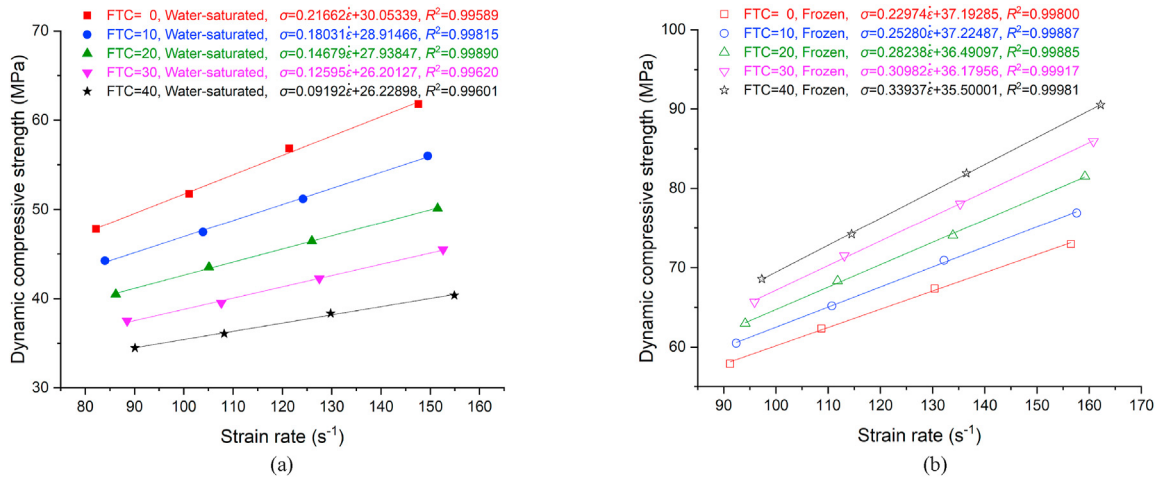

Fig. 11. Relationships between dynamic compressive stress and number of F-T cycles: (a) Water-saturated specimens, and (b) Frozen specimens.

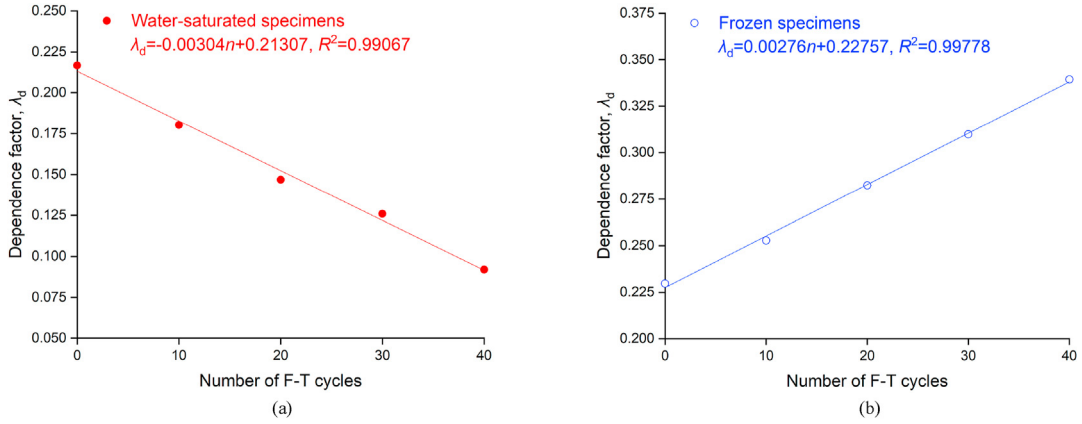

Fig. 12. Relationships between λ_d and the number of F-T cycles: (a) Water-saturated specimens, and (b) Frozen specimens.

analysis, the dependence factors of water-saturated and frozen sandstone specimens are determined by

$$\lambda_d(n) = -0.00304n + 0.21307 \quad \left(R^2 = 0.99067\right) \tag{9}$$

$$\lambda_d(n) = 1.88123n + 0.22757 \quad \left(R^2 = 0.99778\right) \tag{10}$$

3.3. Evolution model of dynamic compressive strength

Based on the exponential decay model of Eq. (4), the strain rate and the number of F-T cycles are used to analyze the dynamic compressive strength equation of water-saturated sandstone specimens. Through regression analysis, the attenuation factor (λ_a) of water-saturated sandstone can be determined by

$$\sigma_{S,(n)} = \sigma_{S,(0)} e^{-(3.55938\dot{\varepsilon}+0.00523)n} \tag{11}$$

Similarly, the intensifying factor (λ_i) of frozen sandstone can be determined as

$$\sigma_{F,(n)} = \sigma_{F,(0)} e^{(1.88123\dot{\varepsilon}+0.00237)n} \tag{12}$$

Fitting the results in Fig. 12a yields the exponential decay model of the determination coefficient of water-saturated sandstone specimens. The final determination coefficient (R_S^2) of the equation for predicting the dynamic compressive strength of water-saturated sandstone specimens is obtained by multiplying this coefficient by the coefficients of the attenuation factor (λ_a) of Eq. (6). Similarly, the fitting results in Fig. 12b yield the determination coefficient of the exponential growth model for frozen sandstone specimens, which is multiplied by the coefficients of the intensifying factor (λ_i) in Eq. (7) to yield the final determination coefficient (R_F^2) of the equation for predicting the dynamic compressive strength of frozen sandstone. Table 5 shows the results, with a high final determination coefficient indicating that the proposed dynamic compressive strength prediction equation well fits the data.

Table 5
Total correlation coefficient of the attenuation factor and intensifying factor.

Water-saturated sandstone specimens			Frozen sandstone specimens		
Strain rate, $\dot{\varepsilon}$ (s^{-1})	Attenuation factor, λ_a	Final determination coefficient of $\sigma_{S,(n)}$, R_S^2	Strain rate, $\dot{\varepsilon}$ (s^{-1})	Intensifying factor, λ_i	Final determination coefficient of $\sigma_{F,(n)}$, R_F^2
86 ± 5	0.00817	0.97418	94 ± 5	0.00421	0.98382
104 ± 5	0.00901	0.97422	111 ± 5	0.00439	0.98231
125 ± 5	0.00982	0.97429	134 ± 5	0.00488	0.98327
152 ± 5	0.01053	0.97371	160 ± 5	0.00541	0.98355

When the dynamic compressive strength of sandstone without F-T cycles is known, this prediction equation can be used to predict the dynamic compressive strength of sandstone after various F-T cycles based on the strain rate.

4. Discussion

4.1. Mesoscopic mechanism of evolution characteristics of dynamic compressive strength

Fig. 13a–d illustrates the process of F-T damage and deterioration. Due to the temperature drop, the pore water inside the rock freezes, and its volume expands by approximately 9%, as shown in Fig. 13a and b. The solid medium shrinks when it is cold, resulting in the generation of a frost heaving force, the development of primary pores and fractures in the rock, the generation of new pores and the destruction of the internal structure of the rock. As shown in Fig. 13c and d, when the temperature rises, the pore ice inside the rock melts into pore water, which then percolates and migrates inside the rock, forming fissure channels to flow and removing part of the cemented materials and mineral particles, increasing the porosity of the rock and causing rock damage.

In this paper, NMR tests were conducted to obtain these change characteristics, and the specimens of Group CE were tracked and tested to measure the change in porosity. The T_2 spectral distribution curves of sandstone specimen CE5, whose porosity is closest to the average value of Group CE after various F-T cycles, are shown in Fig. 14. The porosity component is the proportion of the corresponding pore size, and the accumulative porosity is the sum of the porosity components of different pore sizes. As the number of F-T cycles increases, the peak value of the T_2 spectrum distribution curves increases, and the porosity accumulation increases. New microcracks with large pores are generated, in addition to the expansion and development of the original internal pores of the rock specimen, i.e. the cumulative damage inside the sandstone specimen increases, and the increase is significant. Therefore, with different degrees of F-T damage, the strength of sandstone specimens is also differently affected.

Fig. 15a and b depicts the mesoscopic structure diagrams of low F-T damage and high F-T damage, respectively, which are used to compare the mesoscopic mechanism of dynamic compressive strength evolution of water-saturated and frozen sandstone specimens. The softening effect of pore water in water-saturated sandstone (Fig. 15c and e) lowers the matrix minerals' specific surface energy and friction coefficient and makes them easier to peel and slide under loads. Dry clay minerals between two pores gradually become water-saturated and turn into pore mud, weakening the mechanical properties of water-saturated sandstone. As the number of F-T cycles increases, the porosity of sandstone specimens and the water content of water-saturated sandstone increase, and the water softening effect intensifies, resulting in a decrease in the dynamic compressive strength of water-saturated sandstone.

Pore ice formed by pore water in frozen sandstone (Fig. 15d and f) (in this process, excess pore water infiltrates into the surface of the specimen and freezes) fills the pores and freezes saturated clay minerals, enhancing the frozen sandstone specimen. The pressure generated by chilled water usually creates cracks between the clay minerals and the matrix minerals (matrix minerals are mainly quartz). The strength of pore ice at the boundary between matrix minerals and clay minerals is lower than the original strength between them. The strength of ice is much lower than that of matrix minerals. Therefore, the strength of frozen sandstone should have decreased with an increase in the number of F-T cycles. However, the test results show the opposite trend because the freezing process freezes and consolidates the wet clay matrix bonded with the skeleton matrix. Kaolinite is a type of clay mineral mainly produced by the natural alteration of feldspar and other silicate minerals. It is also a type of water-borne aluminosilicate that absorbs water when drying. During the F-T cycles, although the matrix minerals slightly decrease, the clay minerals increase. After freezing, the clay minerals and matrix minerals are consolidated due to freezing, forming

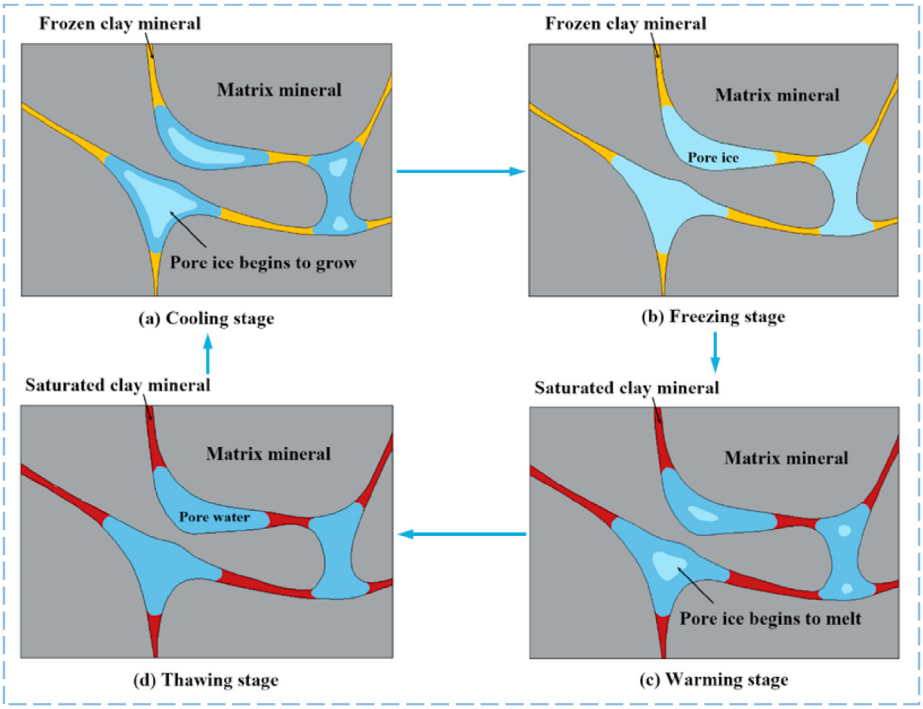

Fig. 13. Mesoscopic mechanism of a complete F-T cycle.

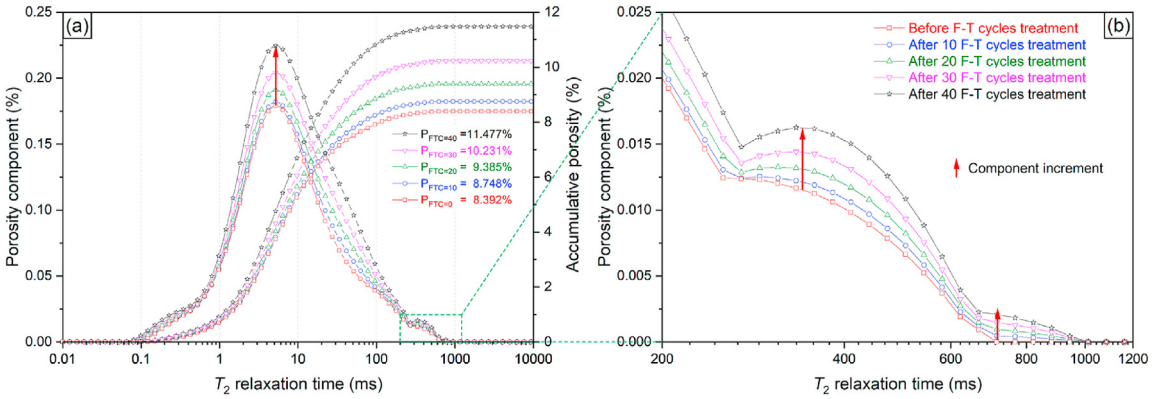

Fig. 14. T_2 spectrum distribution curves of sandstone specimens of Group CE for different numbers of F-T cycles.

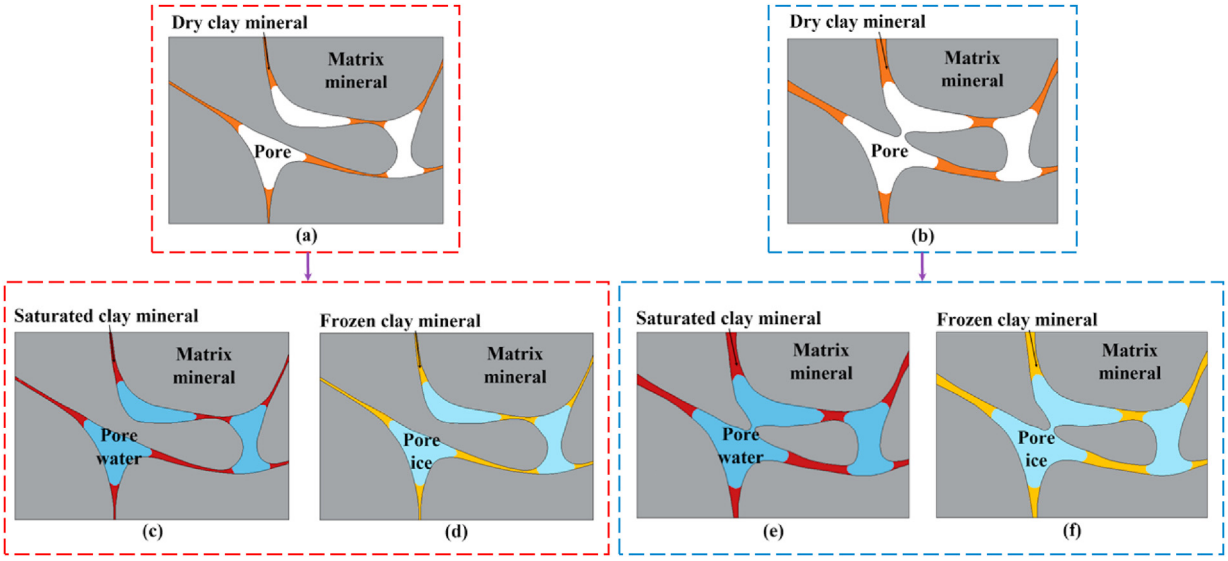

Fig. 15. Mesoscopic mechanism of dynamic compressive strength evolution for different types of damage: (a) Low F-T damage, (b) High F-T damage, (c) Water-saturated specimen under low F-T damage, (d) Frozen specimen under low F-T damage, (e) Water-saturated specimen under high F-T damage, and (f) Frozen specimen under high F-T damage.

a new whole, and the strength of this new matrix product accordingly increases. Before the number of F-T cycles does not exceed a critical point (i.e. before reaches a critical point in a simulated reality, destroying the skeleton matrix), the increase in the number of F-T cycles causes an increase in porosity and a decrease in water saturation strength. However, the frozen compressive strength will increase instead. Until the critical point is reached, the frozen compressive strength will be sharply reduced after the matrix mineral is completely destroyed, making it easier to destroy. When the external force suddenly increases, the ice will show brittle and elastic characteristics but no plastic characteristics. During the experiment, the sandstone was saturated with water and wrapped with plastic film for the freezing test. As the density of ice is less than that of water, a layer of ice film will form on the sandstone surface after water seepage and freezing in the impact load test. In the high load impact test, with an increase in the number of F-T cycles, the porosity increases, and the plastic property of frozen sandstone slightly decreases, while the brittleness and elasticity increase, which indirectly increases the compressive strength of frozen sandstone. Therefore, the strength of frozen sandstone increases with increasing porosity before the matrix minerals are completely destroyed. We attribute this phenomenon to the consolidation effect of sandstone in the unfrozen environment.

The mesoscopic mechanism of a complete F-T cycle is qualitatively analyzed in Figs. 13 and 15, and it can be inferred that the change in pore water and pore ice (as well as the consolidation effect during freezing) caused by micropore evolution is the main reason for the difference in dynamic compressive strength evolution laws between water-saturated sandstone and frozen sandstone.

4.2. Correlation analysis of the increasing rate of porosity and relative dynamic compressive strength (RDCS)

To quantitatively analyze the evolution law of the dynamic compressive strength of water-saturated and frozen sandstone specimens, a correlation analysis of the dynamic compressive strength of sandstone is carried out. The apparent effect of the F-T cycles on rock is the increasing rate of porosity that directly reflects the F-T damage changes in specimens. Eq. (13) expresses the change in porosity and the increasing rate of porosity:

$$\mu_P = \frac{P_{(n)} - P_{(0)}}{P_{(0)}} \tag{13}$$

where μ_P is the increasing rate of porosity; and $P_{(n)}$ and $P_{(0)}$ are the porosities of sandstone after n F-T cycles and before F-T cycles, respectively.

The porosity change of sandstone specimens was tested using NMR and is shown in Table 6 and Fig. 16. The porosity increasing rate of sandstone specimens increases with the number of F-T cycles.

Fig. 17 shows the fitting curves between RDCS of sandstone specimens and the increasing rate of porosity. There is a strong correlation between RDCS and the porosity increasing rates of water-saturated sandstone and frozen sandstone with different F-T cycles, as determined by fitting and correlation analysis of the experimental data. As shown in Fig. 17a, the RDCS of water-saturated sandstone decreases with the increasing rate of porosity. It can be considered that the increase in pore water causes a decrease in the strength of the water-saturated sandstone, which is consistent with the evolution mechanism of the dynamic strength of the water-saturated sandstone shown in Fig. 15, i.e. the softening effect of water intensifies its damage of compressive strength. However, the relative compressive strength of frozen sandstone specimens increases with porosity, as shown in Fig. 17b, which is consistent with the mesoscopic mechanism of dynamic compressive strength evolution of frozen sandstone caused by the increase in pore ice shown in Fig. 15.

Table 6
NMR experimental results.

Number of F-T cycles	Average porosity (%)		Increasing rate (%)
	Before F-T	After F-T	
0	8.308 (−0.046)		
10	8.333 (−0.049)	8.797 (−0.048)	5.57
20	8.358 (−0.052)	9.488 (−0.051)	13.52
30	8.384 (−0.055)	10.366 (−0.056)	23.65
40	8.409 (−0.06)	11.487 (−0.062)	36.6

Note: The numbers included in the round brackets are the population standard deviations.

4.3. Deficiencies and prospects

In actual projects in cold regions, repeated F-T cycles will cause obvious frost heave of rocks, resulting in many geotechnical engineering disasters (Lai et al., 2000; Matsuoka, 2008; Ruedrich et al., 2011; Krautblatter et al., 2013; Al-Omari et al., 2015; Huang et al., 2020; Weng et al., 2021; Zhang et al., 2022). Existing studies (Altindag et al., 2004; Yavuz, 2011; Fener and İnce, 2015; Khanlari et al., 2015; Ince and Fener, 2016; Momeni et al., 2016; Wang et al., 2016a, b; Cui et al., 2017; Fang et al., 2018; Zhang et al.,

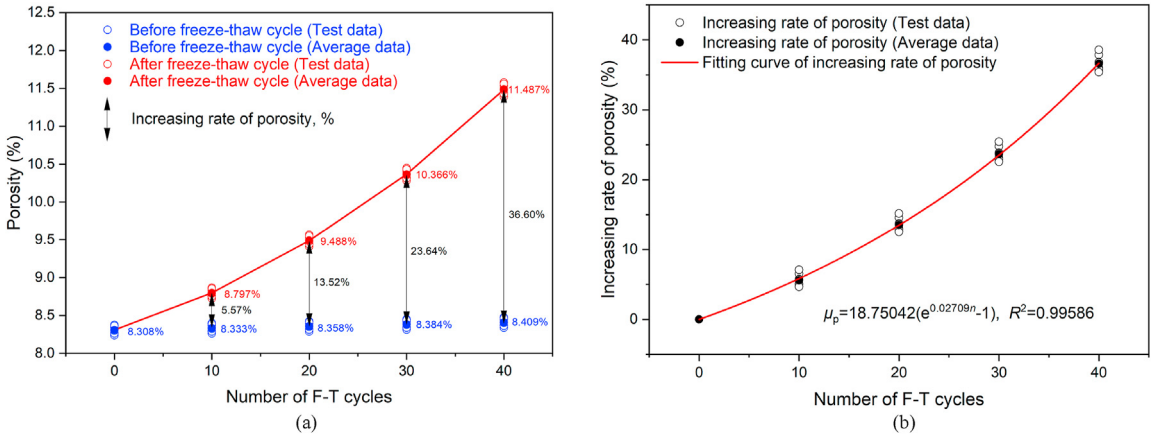

Fig. 16. Evolution curves of (a) porosity and (b) its increasing rate of sandstone specimens in Group CE for different numbers of F-T cycles.

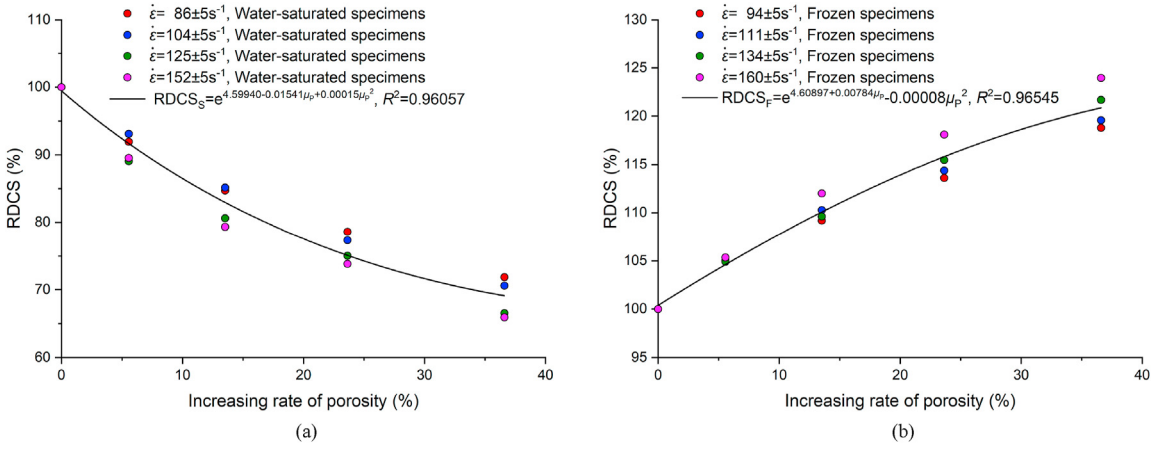

Fig. 17. Relationships between RDCS and increasing rate of porosity: (a) Water-saturated specimens, and (b) Frozen specimens.

2019a; Gao et al., 2021) only focussed on the mechanical properties of rock after F-T cycle treatment and disregarded the effects of rock states on mechanical properties. There is a lack of research on rocks in different states after F-T cycle treatment (some of these studies did not indicate whether the specimens are dry or water-saturated, while other studies only used dry or water-bearing specimens). To investigate the effects of water-saturated and frozen states on the dynamic properties of rocks, sandstone specimens in the seasonally frozen soil layer of the Jiama copper mine slope were obtained, and then F-T cycle tests and SHPB tests were carried out. The dynamic compressive strength prediction model based on F-T cycles and strain rate has a final determination coefficient greater than 0.97, which shows that the model can effectively predict the dynamic compressive strength of water-saturated and frozen sandstone specimens.

However, note that the water-saturated and frozen states describe a relatively ideal situation, while the actual engineering rocks are often in a mixed state of frozen and water-saturated, with different water and ice contents. In such a mixed state, the mechanical properties and mesoscopic mechanism of dynamic compressive strength evolution are more complex than the ideal water-saturated and frozen states. This study aims to analyze the effects of water-saturated and frozen sandstone with various F-T cycles to explain the effects of the frozen stage on the mechanical properties and mesoscopic damage of rocks. The difference in dynamic properties between frozen sandstone and water-saturated sandstone indicates that the existing mechanical models are inaccurate in describing the mechanical behavior of rock excavation in cold regions. Future research can be carried out based on different water and ice contents and the conversion rates of water and ice in the pores so that the test conclusion could be closer to the actual engineering situation.

In addition, we propose two directions for future studies. The first direction is the influence of different clay mineral contents on the compressive strength of frozen rock. The sandstone used in this test has a high content of clay minerals, and the frozen products of clay minerals and water may have a great impact on the strength of the sandstone. For sandstone or other types of rocks with low clay mineral content, we may conclude that the compressive strength of frozen rocks will decrease with an increase in the number of F-T cycles. The second direction is that the sandstone used in this test has only 40 F-T cycles at most, which is relatively low. We suspect that when the critical point is reached and the matrix minerals are destroyed, the strength of frozen sandstone will sharply decline (i.e. after more than 40 F-T cycles, the strength of frozen sandstone will have a turning point). However, these tests need to be designed and verified in a new round of tests, which is also a direction that can be explored.

5. Conclusions

In this paper, dynamic compression tests on sandstone specimens with different numbers of F-T cycles (i.e. 0, 10, 20, 30 and 40) were performed. The dynamic characteristics of water-saturated and frozen sandstone specimens were investigated. The following findings are drawn:

(1) The concepts of the attenuation factor (λ_a), intensifying factor (λ_i) and dependence factor (λ_d) are introduced. With increasing strain rate, the attenuation factor (λ_a) of water-saturated sandstone and intensifying factor (λ_i) of frozen sandstone exhibit linear growth. As the number of F-T cycles increases, the dependence factor (λ_a) of water-saturated sandstone linearly decreases, while that of frozen sandstone linearly increases.

(2) The prediction equations of the dynamic compressive strengths of water-saturated and frozen sandstone specimens considering the strain rate effect and the number of F-T cycles are obtained, respectively, i.e. $\sigma_{S,(n)} = \sigma_{S,(0)}e^{-(3.55938\dot{\varepsilon}+0.00523)n}$ and $\sigma_{F,(n)} = \sigma_{F,(0)}e^{(1.88123\dot{\varepsilon}+0.00237)n}$. The proposed dynamic compressive strength prediction equation well fits the data, as evidenced by the high final determination coefficient value. The prediction equation can be used to predict the dynamic compressive strength of sandstone after various F-T cycles based on the strain rate.

(3) The mesoscopic mechanism of the dynamic compressive strength evolution of water-saturated and frozen sandstone specimens is investigated. The water softening effect causes the dynamic compressive strength of water-saturated sandstone to decrease, whereas the consolidation effect of pore ice on moist clay minerals and matrix minerals during freezing causes the dynamic compressive strength of frozen sandstone to increase.

(4) The RDCS of water-saturated sandstone is related to the increasing rate of porosity under the F-T cycles. After fitting the experimental data of the RDCS with increasing rate of porosity for water-saturated and frozen sandstone specimens after different numbers of F-T cycles, a strong correlation between them is observed.

Declaration of competing interest

The authors declare that they have no known competing financial interests or personal relationships that could have appeared to influence the work reported in this paper.

Acknowledgments

This work was supported by the Hunan Provincial Natural Science Foundation of China (Grant No. 2020JJ4704) and the Fundamental Research Funds for the Central Universities of Central South University, China (Grant Nos. 2021zzts0881 and 2021zzts0279).

References

Al-Omari, A., Beck, K., Brunetaud, X., Török, Á., Al-Mukhtar, M., 2015. Critical degree of saturation: a control factor of freeze–thaw damage of porous limestones at Castle of Chambord. France. Eng. Geol. 185, 71–80.
Altindag, R., Alyildiz, I.S., Onargan, T., 2004. Mechanical property degradation of ignimbrite subjected to recurrent freeze-thaw cycles. Int. J. Rock Mech. Min. Sci. 6 (41), 1023–1028.
Cui, K., Wu, G., Wang, X., Chen, W., 2017. Behaviour of slate following freeze–thaw and dry–wet processes. Q. J. Eng. Geol. Hydrogeol. 50 (2), 117–125.
Fang, X., Xu, J., Wang, P., 2018. Compressive failure characteristics of yellow sandstone subjected to the coupling effects of chemical corrosion and repeated freezing and thawing. Eng. Geol. 233, 160–171.
Fener, M., İnce, İ., 2015. Effects of the freeze–thaw (F–T) cycle on the andesitic rocks (Sille-Konya/Turkey) used in construction building. J. Afr. Earth Sci. 109, 96–106.
Gao, F., Xiong, X., Zhou, K.P., Li, J.L., Shi, W.C., 2019. Strength deterioration model of saturated sandstone under freeze-thaw cycles. Rock Soil Mech. 40, 926–932, 03.
Gao, F., Xiong, X., Xu, C., Zhou, K., 2021. Mechanical property deterioration characteristics and a new constitutive model for rocks subjected to freeze-thaw process. Int. J. Rock Mech. Min. Sci. 140, 104642.
Huang, S., Lu, Z., Ye, Z., Xin, Z., 2020. An elastoplastic model of frost deformation for the porous rock under freeze-thaw. Eng. Geol. 278, 105820.
İnce, İ., Fener, M., 2016. A prediction model for uniaxial compressive strength of deteriorated pyroclastic rocks due to freeze–thaw cycle. J. Afr. Earth Sci. 120, 134–140.
Jamshidi, A., Nikudel, M.R., Khamehchiyan, M., 2013. Predicting the long-term durability of building stones against freeze–thaw using a decay function model. Cold Reg. Sci. Technol. 92, 29–36.
Ke, B., Zhou, K., Xu, C., Deng, H., Li, J., Bin, F., 2018. Dynamic mechanical property deterioration model of sandstone caused by freeze–thaw. Rock Mech. Rock Eng. 51 (9), 2791–2804.

Khanlari, G., Sahamieh, R.Z., Abdilor, Y., 2015. The effect of freeze–thaw cycles on physical and mechanical properties of Upper Red Formation sandstone, central part of Iran. Arabian J. Geosci. 8 (8), 5991–6001.
Krautblatter, M., Funk, D., Günzel, F.K., 2013. Why permafrost rocks become unstable: a rock–ice mechanical model in time and space. Earth Surf. Process. Landforms 38 (8), 876–887.
Lai, Y.M., Wu, H., Wu, Z.W., Liu, S.Y., Den, X.J., 2000. Analytical viscoelastic solution for frost force in cold-region tunnels. Cold Reg. Sci. Technol. 31, 227–234.
Li, X.B., Lok, T.S., Zhao, J., 2005. Dynamic characteristics of granite subjected to intermediate loading rate. Rock Mech. Rock Eng. 38 (1), 21–39.
Li, X., Zhou, Z., Lok, T.S., Hong, L., Yin, T., 2008. Innovative testing technique of rock subjected to coupled static and dynamic loads. Int. J. Rock Mech. Min. Sci. 45 (5), 739–748.
Li, J., Kaunda, R.B., Zhou, K., 2018. Experimental investigations on the effects of ambient freeze-thaw cycling on dynamic properties and rock pore structure deterioration of sandstone. Cold Reg. Sci. Technol. 154, 133–141.
Liu, H., Niu, F.J., Xu, Z.Y., Lin, Z.J., Xu, J., 2011. Acoustic experimental study of two types of rock from the Tibetan Plateau under the condition of freeze–thaw cycles. Sci. Cold Arid Reg. 4, 21–27.
Liu, Q., Huang, S., Kang, Y., Liu, X., 2015. A prediction model for uniaxial compressive strength of deteriorated rocks due to freeze–thaw. Cold Reg. Sci. Technol. 120, 96–107.
Liu, C., Deng, H., Zhao, H., Zhang, J., 2018. Effects of freeze-thaw treatment on the dynamic tensile strength of granite using the Brazilian test. Cold Reg. Sci. Technol. 155, 327–332.
Liu, C., Wang, D., Wang, Z., Ke, B., Li, P., Yu, S., 2021. Dynamic splitting tensile test of granite under freeze-thaw. Soil Dynam. Earthq. Eng. 140, 106411.
Luo, X., Jiang, N., Zuo, C., Dai, Z., Yan, S., 2014. Damage characteristics of altered and unaltered diabases subjected to extremely cold freeze–thaw cycles. Rock Mech. Rock Eng. 47 (6), 1997–2004.
Ma, Q., Ma, D., Yao, Z., 2018. Influence of freeze-thaw cycles on dynamic compressive strength and energy distribution of soft rock specimen. Cold Reg. Sci. Technol. 153, 10–17.
Matsuoka, N., 2008. Frost and rockwall erosion in the southeastern Swiss Alps: long-term (1994–2006) observations. Geomorphology 99 (1–4), 353–368.
Momeni, A., Abdilor, Y., Khanlari, G.R., Heidari, M., Sepahi, A.A., 2016. The effect of freeze–thaw cycles on physical and mechanical properties of granitoid hard rocks. Bull. Eng. Geol. Environ. 75 (4), 1649–1656.
Mutlutürk, M., Altindag, R., Türk, G., 2004. A decay function model for the integrity loss of rock when subjected to recurrent cycles of freezing–thawing and heating–cooling. Int. J. Rock Mech. Min. Sci. 41 (2), 237–244.
Niu, C., Zhu, Z., Zhou, L., et al., 2021. Study on the microscopic damage evolution and dynamic fracture properties of sandstone under freeze-thaw cycles. Cold Reg. Sci. Technol. 191, 103328.
Okubo, S., Fukui, K., 1996. Complete stress-strain curves for various rock types in uniaxial tension. Int. J. Rock Mech. Min. Sci. 33 (6), 549–556.
Ruedrich, J., Kirchner, D., Siegesmund, S., 2011. Physical of building stones induced by freeze–thaw action: a laboratory long-term study. Environ. Earth Sci. 63 (7), 1573–1586.
SL/T 264-2020, 2020. Code for Rock Tests in Water and Hydropower Projects. Ministry of Water Resources of the People's Republic of China, Beijing, China.
SY/T 6351-1998, 1998. Laboratory Measurement of Acoustic Properties on Rock. China National Petroleum Corporation, Beijing, China.
SY/T 6490-2007, 2007. Specification for Normalization Measurement of Core NMR Parameter in Laboratory. National Development and Reform Commission, Beijing, China.
Tan, X., Chen, W., Yang, J., Cao, J., 2011. Laboratory investigations on the mechanical properties degradation of granite under freeze–thaw cycles. Cold Reg. Sci. Technol. 68 (3), 130–138.
Török, Á., Ficsor, A., Davarpanah, M., Vásárhelyi, B., 2019. Comparison of mechanical properties of dry, saturated and frozen porous rocks. In: IAEG/AEG Annual Meeting Proceedings. Springer, San Francisco, California, USA, pp. 113–118.
Ulusay, R., 2015. The ISRM Suggested Methods for Rock Characterization, Testing and Monitoring: 2007-2014. Springer, Cham, Switzerland.
Wang, P., Xu, J., Liu, S., Liu, S., Wang, H., 2016a. A prediction model for the dynamic mechanical degradation of sedimentary rock after a long-term freeze-thaw: considering the strain-rate effect. Cold Reg. Sci. Technol. 131, 16–23.
Wang, P., Xu, J., Liu, S., Wang, H., Liu, S., 2016b. Static and dynamic mechanical properties of sedimentary rock after freeze-thaw or thermal shock. Eng. Geol. 210, 148–157.
Wang, L., Li, N., Qi, J., Tian, Y., Xu, S., 2019. A study on the physical index change and triaxial compression test of intact hard rock subjected to freeze-thaw cycles. Cold Reg. Sci. Technol. 160, 39–47.
Weng, L., Wu, Z., Taheri, A., Liu, Q., Lu, H., 2020. Deterioration of dynamic mechanical properties of granite due to freeze-thaw: considering the effects of moisture conditions. Cold Reg. Sci. Technol. 176, 103092.
Weng, L., Wu, Z., Liu, Q., Chu, Z., Zhang, S., 2021. Evolutions of the unfrozen water content of saturated sandstones during freezing process and the freeze-induced damage characteristics. Int. J. Rock Mech. Min. Sci. 142, 104757.
Yavuz, H., 2011. Effect of freeze–thaw and thermal shock on the physical and mechanical properties of an andesite stone. Bull. Eng. Geol. Environ. 70 (2), 187–192.
Zhang, J., Fu, H., Huang, Z., Wu, Y., Chen, W., Shi, Y., 2019a. Experimental study on the tensile strength and failure characteristics of transversely isotropic rocks after freeze-thaw cycles. Cold Reg. Sci. Technol. 163, 68–77.
Zhang, J., Deng, H., Taheri, A., Ke, B., Liu, C., 2019b. Deterioration and strain energy development of sandstone under quasi-static and dynamic loading after freeze-thaw cycles. Cold Reg. Sci. Technol. 160, 252–264.
Zhang, Q., Liu, Y., Dai, F., Jiang, R., 2022. Experimental assessment on the fatigue mechanical properties and fracturing mechanism of sandstone exposed to freeze-thaw treatment and cyclic uniaxial compression. Eng. Geol. 306, 106724.
Zhou, K., Li, B., Li, J., Deng, H., Bin, F., 2015. Microscopic damage and dynamic mechanical properties of rock under freeze–thaw environment. Trans. Nonferrous Metals Soc. China 25 (4), 1254–1261.

Xin Xiong obtained his BSc degree in Mining Engineering from Northeastern University, Shenyang, China, in 2016, and his MSc degree in Mining Engineering from Central South University, Changsha, China, in 2019. Now, he is a PhD candidate in Mining Engineering at Central South University. His research interests include (1) Mining method and technology of metal mine, (2) Freeze-thaw rock mechanics, and (3) Constitutive model of rock subjected to multi-field coupling. Up to now, he has published 8 papers as the first author or corresponding author, and hold 9 patents as the second or third inventor.